A HIGH SPATIAL RESOLUTION STUDY OF THE $\lambda = 3$ mm CONTINUUM OF ORION-KL

D. N. Friedel[1] and S. L. Widicus Weaver[2]
[1] Department of Astronomy, 1002 W. Green St., University of Illinois, Urbana IL 61801, USA; friedel@astro.illinois.edu
[2] Department of Chemistry, Emory University, Atlanta, GA 30322, USA; susanna.widicus.weaver@emory.edu

ABSTRACT

Recent interferometric observations have called into question the traditional view of the Orion-KL region, which displays one of the most well-defined cases of chemical differentiation in a star-forming region. Previous lower-resolution images of Orion-KL show emission signatures for oxygen-bearing organic molecules toward the Orion Compact Ridge and emission for nitrogen-bearing organic molecules toward the Orion Hot Core. However, more recent observations at higher spatial resolution indicate that the bulk of the molecular emission arises from many smaller, compact clumps that are spatially distinct from the traditional Hot Core and Compact Ridge sources. It is this type of observational information that is critical for guiding astrochemical models, as the spatial distribution of molecules and their relation to energetic sources will govern the chemical mechanisms at play in star-forming regions. We have conducted millimeter-imaging studies of Orion-KL with various beam sizes using the Combined Array for Research in Millimeter-Wave Astronomy in order to investigate the continuum structure. These $\lambda = 3$ mm observations have synthesized beam sizes of $\sim 0\rlap{.}''5$–$5\rlap{.}''0$. These observations reveal the complex continuum structure of this region, which stands in sharp contrast to the previous structural models assumed for Orion-KL based on lower spatial resolution images. The new results indicate that the spatial scaling previously used in determination of molecular abundances for this region are in need of complete revision. Here we present the results of the continuum observations, discuss the sizes and structures of the detected sources, and suggest an observational strategy for determining the proper spatial scaling to accurately determine molecular abundances in the Orion-KL region.

Key words: astrochemistry – ISM: individual objects (Orion-KL) – radio continuum: ISM

Online-only material: color figure

1. INTRODUCTION

The Orion-KL region is the closest (~ 414 pc) site of massive star formation to Earth (Menten et al. 2007). There are several cloud components (e.g., Hot Core, Compact Ridge, extended ridge, and plateau) that are associated with Orion-KL, and these sources have varying chemical and physical properties (e.g., Blake et al. 1987). The most chemically rich components, including the Hot Core, IRc7, IRc6, and IRc5, are separated by less than ~ 4000 AU (projected on the sky). Emission lines from large oxygen-bearing species (e.g., methyl formate [$HCOOCH_3$] and dimethyl ether [$(CH_3)_2O$]) have been observed primarily toward IRc5 and IRc5 in the Compact Ridge, while emission from large nitrogen-bearing species (e.g., ethyl cyanide [C_2H_5CN]) is observed toward the Hot Core and IRc7 (Friedel & Snyder 2008).

The chemical pathways leading to the formation of complex organic molecules in regions such as Orion-KL are very poorly understood (e.g., Quan & Herbst 2007). It was once assumed that gas-phase ion–molecule reactions in hot cores drive most of the organic chemistry observed in interstellar clouds, but it has since been shown that such reactions are inefficient for producing many of the most highly abundant molecules observed in these regions (Garrod et al. 2008). Instead, it is thought that energetic processing of interstellar ices is a likely driving force that dramatically influences interstellar chemistry (Garrod et al. 2008; Laas et al. 2011). The spatial distribution of a given molecular species relative to the position of energetic sources (i.e., shock fronts, photodissociation regions, stellar objects, etc.) might offer clues to the processes that drive its formation. Previous interferometric observations of Orion-KL (see Liu et al. 2002 for an example) used older generation interferometers that provided insufficient spatial resolution to distinguish these individual regions and pinpoint possible correlations between a particular

molecule and any given source. Friedel & Snyder (2008) reported higher spatial resolution observations of several organic molecules toward Orion-KL at $\lambda = 1$ mm. The results of these observations indicate a relationship between the type of physical environment and the chemistry observed in Orion-KL. Other recent observations targeting methyl formate at a similar spatial resolution reveal a highly complicated source structure (Favre et al. 2011). These recent results warrant further investigation at even higher spatial resolution.

To this end, we have carried out interferometric observations at the Combined Array for Research in Millimeter-Wave Astronomy (CARMA) over a range of spatial resolutions toward Orion-KL to more fully investigate the spatial extent of molecules in the region. These observations targeted specific emission lines of several complex organic molecules. Continuum observations at $\lambda = 3$ mm were conducted to explore source structure and size. Below we overview these observations, present the continuum images at several beam sizes, and discuss the implications of these results for the standard spatial models assumed when determining molecular abundances for the Orion-KL region.

2. OBSERVATIONS

The observations were conducted in 2007 December, 2008 July, 2009 January, and 2010 April with the CARMA observatory in its B, D, A, and C configurations, respectively. These observations included two 7 hr tracks in B configuration, one 6 hr track in D configuration, four 5–6 hr tracks in A configuration, and three 4.5 hr tracks in C configuration. The observations have a phase center of α(J2000) $= 05^h 35^m 14\rlap{.}^s 35$ and δ(J2000) $= -05°22'35\rlap{.}''0$. The typical synthesized beams are $\sim 5\rlap{.}''9 \times 4\rlap{.}''8$ (D configuration), $\sim 2.2 \times 2\rlap{.}''0$ (C configuration), $\sim 1\rlap{.}''1 \times 0\rlap{.}''9$ (B configuration), and $\sim 0.4 \times 0\rlap{.}''35$ (A configuration).

The $u - v$ coverage of the observations gives projected baselines of 3.0–35.3 kλ (10–118 m, D configuration), 3.9–91.0 kλ (13–304 m, C configuration), 21.8–257.5 kλ (73–860 m, B configuration), and 38.0–467.2 kλ (127–1560 m, A configuration). By observing over such a wide range of $u - v$ coverage, only structures larger than $\sim 30''$ are resolved out. Each arcsecond is equivalent to ~ 414 AU at the distance of Orion-KL.

The correlator was configured with six 31 MHz wide windows for continuum and spectral lines (three in each sideband) for the observations conducted in the B and D configurations. Each window had 63 channels with a channel spacing of 488 kHz (~ 1.4 km s^{-1}). The continuum images were constructed from both line-free windows and windows containing flagged lines. Uranus and Mars were used as flux density calibrators, and 0541-056 was used to calibrate the antenna-based gains. For two of the A configuration tracks, the correlator was configured with four 31 MHz wide windows and two 500 MHz wide windows (three in each sideband). The correlator configuration for the third A configuration track was two 31 MHz bands and four 500 MHz bands, while the fourth track was configured with four 31 MHz bands and two 62 MHz bands. The antenna-based gain calibration was done by self-calibrating on the SiO maser in source I at 86.243 GHz. The solution was then bootstrapped to the other bands. Phase offsets between each band and the SiO band were calculated and removed by using observations of 0607-085. As all available flux calibrators were heavily resolved in A configuration, the amplitude gains were calculated by comparing previously measured fluxes of 0607-085 with these observations. The absolute amplitude calibrations of 0541-056 and 0607-085 are accurate to within $\sim 20\%$. The internal noise source was used to correct the passbands of each 31 MHz window, and observations of 0423-013 were used to correct the passbands of the 500 and 62 MHz windows. The data were calibrated, continuum subtracted, and imaged using the MIRIAD software package (Sault et al. 1995). Note that the flux of the point source BN (see Section 3) is similar across all array configurations, indicating that the accuracy of the absolute flux calibration between the different tracks is better than 95%.

3. RESULTS AND DISCUSSION

Figure 1 shows the $\lambda = 3$ mm continuum of Orion-KL from the A, B, C, and D array configuration observations. The noise levels are 290 μJy beam^{-1}, 2.4 mJy beam^{-1}, 2.2 mJy beam^{-1}, and 1.8 mJy beam^{-1}, respectively, and the synthesized beams for each array configuration are shown in the lower left corner of each panel. The large-scale structures seen in the 5$''$ resolution observations are resolved into several dozen sources as the beam area decreases by two orders of magnitude. The strongest emission peak in the A and B configuration maps arises from source BN, whereas the peak of the emission in the C and D configuration maps is closely associated with the Hot Core. This indicates that, while there are numerous individual sources, the bulk of the continuum emission is coming from more extended regions.

Figure 2 shows a portion of the $\lambda = 3$ mm B configuration continuum (contours) overlaid on a gray-scale *Hubble*/NICMOS 2 μm image[3] of the same region. Sources of interest have been labeled for reference. Most of the millimeter continuum emission does not coincide with infrared active regions, but appears

---

[3] Based on observations made with the NASA/ESA *Hubble Space Telescope*, obtained from the data archive at the Space Telescope Science Institute. STScI is operated by the Association of Universities for Research in Astronomy, Inc. under NASA contract NAS 5-26555.
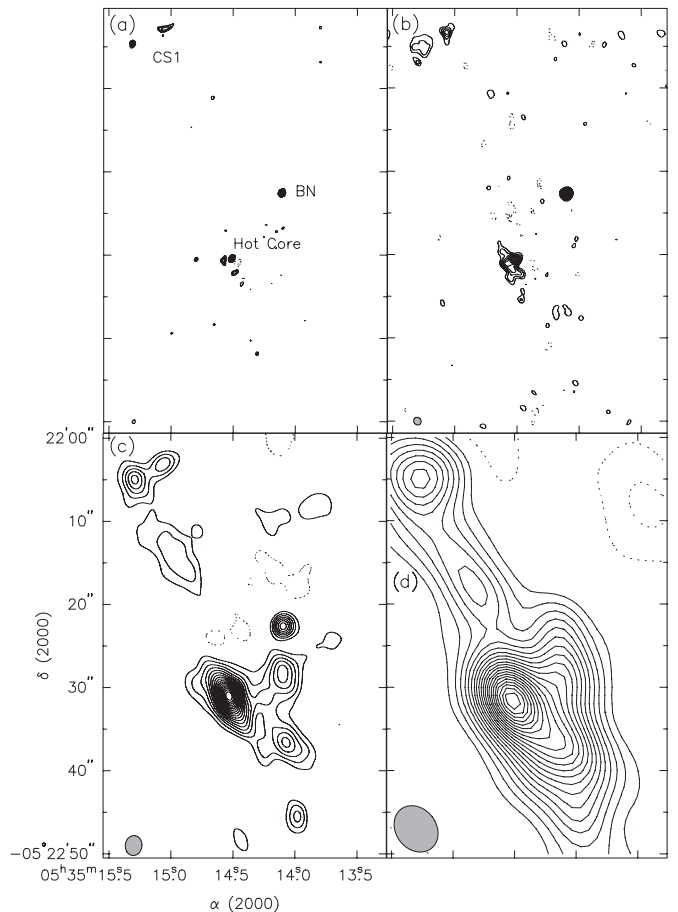
Figure 1. Continuum maps of Orion-KL at $\lambda = 3$ mm. (a) CARMA A configuration map, with contours at $\pm 12\sigma$, $\pm 18\sigma$, $\pm 24\sigma$, ... ($\sigma = 290 \,\mu$Jy beam^{-1}); (b) B configuration map, with contours at $\pm 6\sigma$, $\pm 9\sigma$, $\pm 12\sigma$, ... ($\sigma = 2.4$ mJy beam^{-1}); (c) C configuration map, with contours at $\pm 9\sigma$, $\pm 15\sigma$, $\pm 21\sigma$, ... ($\sigma = 2.2$ mJy beam^{-1}); and (d) D configuration map, with contours at $\pm 12\sigma$, $\pm 24\sigma$, $\pm 36\sigma$, ... ($\sigma = 1.8$ mJy beam^{-1}). Objects of note are labeled in the A configuration panel. The synthesized beam size is shown in the lower left-hand corner of each panel.

to be anti-correlated with most of the sources; the primary exception to this trend is source BN. Here we provide brief descriptions of previously identified infrared and millimeter sources of interest:

BN. A star with the highest $\lambda = 3$ mm point source flux in the region (89 mJy beam^{-1}). This source is also very bright in the infrared (see Figure 2).

Hot Core/I. A site of high-mass star formation that is the traditional location of N-bearing molecules. Source I ($\sim 0.''5$ south of the hot core) is located at the center of the SiO masers (Menten & Reid 1995).

Compact Ridge. A region of stellar outflow interacting with the ambient cloud. This source is the traditional location of O-bearing molecules in the region. Friedel & Snyder (2008) noted that most of the compact emission comes from other sources. No continuum emission above the 3σ level was detected from this region in any of our observations.

SMA1. A high-mass protostellar source (Beuther et al. 2006).

n. A Herbig Ae/Be or mid-B star with a luminosity of $\sim 2000 \, L_\odot$ (Greenhill et al. 2004). There is also an NH$_3$

Figure 2. B configuration continuum image at $\lambda = 3$ mm for the Orion-KL region overlaid on a $2\,\mu$m *Hubble*/NICMOS image. Contours are 4σ, 6σ, 9σ, 12σ, ... ($\sigma = 2.4$ mJy beam^{-1}). Sources of interest have been labeled. Stars are labeled next to their positions and all other sources are noted with labels on their central positions unless indicated with a line.

peak, indicating a high ($>10^7$ cm^{-3}) density (Migenes et al. 1989). Weak emission ($\sim$10 mJy beam^{-1}) is seen toward this source in the B configuration results.

p. A star which is detected both in the infrared and optical (Simpson et al. 2006), with no detected $\lambda = 3$ mm continuum.

k. A star which is detected both in the infrared and optical (Simpson et al. 2006), with no detected $\lambda = 3$ mm continuum.

v. A star which is detected both in the infrared and optical (Simpson et al. 2006), with no detected $\lambda = 3$ mm continuum.

IRc3, 4, and 5. These are objects thought to be reflection nebulae being illuminated by IRc2 (nearly coincident with source I; Simpson et al. 2006). There is no significant NH$_3$ emission seen toward any of these sources (Migenes et al. 1989). There is no detected continuum emission above 3σ toward IRc3, while a weak $\sim$9 mJy beam^{-1} peak is detected toward IRc4. An apparent double-lobed continuum emission peak is centered in close proximity to IRc5.

IRc6. There is notable $\lambda = 3$ mm continuum emission coming from the region between IRc3 and IRc6. Friedel & Snyder (2008) also detected notable $\lambda = 1$ mm continuum from this region.

IRc7. This source is thought to contain an embedded young stellar object (YSO; Simpson et al. 2006) and has a strong NH$_3$ peak, indicating high density (Migenes et al. 1989). However, there is no detected continuum emission above 3σ. Friedel & Snyder (2008) reported weak $\lambda = 1$ mm continuum from this source.

IRc20. Little is known of this object because of its weak emission and proximity to the very bright BN emission.

CB4. A binary with no detected $\lambda = 3$ mm continuum.

Figure 3 shows the A configuration continuum with sources labeled. This is the most sensitive $\lambda = 3$ mm map of this region to date, with a noise level of 290 μJy beam^{-1}. The coordinates and source properties from the labeled sources in the map are given in Table 1. The first column gives the corresponding source ID from the map; the second and third columns give the coordinates; the fourth, fifth, and sixth columns give the deconvolved source size, position angle, and peak flux; and the seventh column gives the results of searching the SIMBAD online database. Figures 3(b) and (c) show contour maps with all A, B, C, and D configuration data combined. The data for Figure 4(a) were mapped using uniform weighting, while the data for Figure 4(b) were mapped using natural weighting. The synthesized beams for each map are shown in the lower left corner of each panel.

Table 2 shows a comparison of the integrated fluxes for the detected sources between the different array configurations. The first column gives the source ID; the second column gives the integrated flux from the D configuration data; the third and fourth columns give the integrated flux and fitted size from the C configuration data; the fifth and sixth columns give the percentage of resolved flux and fitted source size from the B configuration data; and the seventh column gives the percentage of resolved flux from the A configuration data. The percentage of resolved flux listed in both cases is in comparison to the C configuration data, as that is the largest beam size with which most of the sources can be resolved. The percentage of resolved flux was determined by convolving the B and A configuration data with the synthesized beam from the C configuration data

3

Table 1
Continuum Sources From the A Configuration

ID	α(J2000)[a]	δ(J2000)	Size[b] ($'' \times ''$)	PA[b] (deg)	Peak Flux[b] (mJy beam^{-1})	SIMBAD Results[c]
C1	$05^h35^m15\overset{s}{.}310$	$-05°22'04\overset{''}{.}680$	0.72×0.33	2.3	10.83 (93)	MM6 (Eisner & Carpenter 2006)
C2	$05^h35^m15\overset{s}{.}047$	$-05°22'02\overset{''}{.}840$	2.1×0.41	−70.4	8.7 (82)	MM5 (Eisner & Carpenter 2006)
C3	$05^h35^m13\overset{s}{.}796$	$-05°22'02\overset{''}{.}711$	0.33×0.3	28.7	3.98 (32)	YSO? (138-203) (O'dell & Wong 1996)
C4	$05^h35^m13\overset{s}{.}796$	$-05°22'06\overset{''}{.}807$	PS[c]		3.97 (31)	YSO (138-207) (Simpson et al. 2006)
C5	$05^h35^m14\overset{s}{.}665$	$-05°22'11\overset{''}{.}061$	0.4×0.29	41.6	4.73 (76)	YSO (147-211) (Doi et al. 2002)
C6	$05^h35^m15\overset{s}{.}156$	$-05°22'17\overset{''}{.}173$	0.48×0.18	−60.0	2.52 (53)	H_2O maser (Gaume et al. 1998)
C7	$05^h35^m14\overset{s}{.}835$	$-05°22'14\overset{''}{.}660$	0.42×0.19	46.5	3.37 (51)	No sources within $2''$ radius
C8	$05^h35^m14\overset{s}{.}129$	$-05°22'13\overset{''}{.}228$	0.64×0.18	74.1	2.84 (40)	Star? (9) (Simpson et al. 2006)
C9	$05^h35^m13\overset{s}{.}782$	$-05°22'17\overset{''}{.}235$	0.66×0.48	−26.8	2.79 (49)	Star? COUP J053513.7-052217 (Simpson et al. 2006)
C10	$05^h35^m13\overset{s}{.}515$	$-05°22'19\overset{''}{.}340$	0.30×0.15	−12.3	3.42 (23)	YSO (135-220) (Simpson et al. 2006)
C11	$05^h35^m14\overset{s}{.}106$	$-05°22'22\overset{''}{.}528$	0.11×0.02	7.3	90.76 (89)	Embedded star (BN) (Becklin & Neugebauer 1967)
C12	$05^h35^m15\overset{s}{.}179$	$-05°22'29\overset{''}{.}431$	0.40×0.06	43.8	3.15 (26)	X-ray source? (Feigelson et al. 2002)
C13	$05^h35^m14\overset{s}{.}556$	$-05°22'27\overset{''}{.}128$	0.97×0.36	−87.8	4.89 (29)	No sources within $2''$ radius
C14	$05^h35^m14\overset{s}{.}253$	$-05°22'27\overset{''}{.}820$	PS[d]		5.27 (44)	IRc6E (Shuping et al. 2004)
C15	$05^h35^m14\overset{s}{.}155$	$-05°22'27\overset{''}{.}193$	0.85×0.38	−47.7	4.9 (20)	IRc6 (Rieke et al. 1973)
C16	$05^h35^m14\overset{s}{.}096$	$-05°22'26\overset{''}{.}734$	PS[d]		4.43 (29)	IRc6N (Gezari et al. 1998)
C17	$05^h35^m14\overset{s}{.}797$	$-05°22'30\overset{''}{.}557$	PS[d]		9.23 (57)	H_2O maser (Gaume et al. 1998)
C18	$05^h35^m14\overset{s}{.}579$	$-05°22'30\overset{''}{.}679$	0.61×0.28	10.8	7.08 (94)	YSO (146-231)/H_2O maser (Simpson et al. 2006; Gaume et al. 1998)
C19	$05^h35^m14\overset{s}{.}614$	$-05°22'28\overset{''}{.}696$	0.59×0.31	−18.2	4.39 (43)	MM24 (Eisner et al. 2008)
C20	$05^h35^m14\overset{s}{.}511$	$-05°22'30\overset{''}{.}397$	PS[d]		50.09 (97)	Source I (Churchwell et al. 1987)
C21	$05^h35^m14\overset{s}{.}488$	$-05°22'32\overset{''}{.}101$	0.87×0.44	−64.7	6.05 (60)	SMA1 (Beuther et al. 2006)
C22	$05^h35^m14\overset{s}{.}431$	$-05°22'33\overset{''}{.}457$	0.70×0.17	−48.1	5.31 (75)	Hot Core
C23	$05^h35^m14\overset{s}{.}278$	$-05°22'30\overset{''}{.}647$	0.47×0.31	−23.4	4.18 (9)	IRc7 (Wynn-Williams et al. 1984)
C24	$05^h35^m14\overset{s}{.}996$	$-05°22'39\overset{''}{.}411$	0.29×0.19	−87.7	5.39 (34)	YSO (150-240) (Lada et al. 2004)
C25	$05^h35^m14\overset{s}{.}850$	$-05°22'44\overset{''}{.}020$	0.35×0.27	−70.3	2.98 (10)	IR source (Luhman et al. 2000)
C26	$05^h35^m14\overset{s}{.}656$	$-05°22'38\overset{''}{.}363$	PS[d]		5.4 (45)	Star?/YSO (149-239) (Lada et al. 2004)
C27	$05^h35^m14\overset{s}{.}519$	$-05°22'44\overset{''}{.}609$	0.68×0.30	−20.9	2.87 (22)	IR source (MLLA 554) (Muench et al. 2002)
C28	$05^h35^m14\overset{s}{.}309$	$-05°22'41\overset{''}{.}839$	e		6.35 (56)	H_2O maser nearby (Gaume et al. 1998)
C29	$05^h35^m14\overset{s}{.}20$	$-05°22'37\overset{''}{.}15$	f			H_2O and OH maser (Braz & Epchtein 1983)
C30	$05^h35^m13\overset{s}{.}988$	$-05°22'44\overset{''}{.}887$	0.91×0.70	53.3	3.46 (33)	MM23 (Eisner & Carpenter 2006)
C31	$05^h35^m13\overset{s}{.}981$	$-05°22'42\overset{''}{.}611$	0.58×0.38	78.2	3.18 (15)	CH_3OH maser (Johnston et al. 1992)

Notes.

[a] Peak coordinates have an uncertainty $\leqslant$ the $\sim0\overset{''}{.}4$ synthesized beam.

[b] Determined from the MIRIAD task IMFIT. Source sizes and position angle given here are the deconvolved values.

[c] Obtained from a coordinate search in the SIMBAD database (http://simbad.harvard.edu/simbad/).

[d] The deconvolution resulted in a point source.

[e] The deconvolution failed, thus no source size is reported.

[f] A reliable fit could not be obtained; the source position is estimated from its peak.

(using the MIRIAD task CONVOL) and comparing the fitted integrated fluxes. Here, 0% resolved out means no missing flux, while 100% means all flux was resolved out. The last row of Table 2 is a combination of all continuum sources C18–C22 as they are unresolved in both the C and D configuration data.

The following is a discussion of the individual continuum sources detected. Any source not listed below was only detected by the A configuration observations, indicating it is a lone point-like source, or that it has a surrounding envelope below our detection threshold.

C1 and C2. Both of these sources appear to be embedded in an extended envelope, on the order of $\sim10''$, with the bulk of the flux surrounding C1. A third of the flux is resolved out by a $2''$ beam, and a total of 63% is resolved out by the subarcsecond beam.

C4. This continuum source appears to be a single point source embedded in a surrounding envelope several arcseconds in diameter, which emits 75% of the flux. This source was undetected in the D configuration observations due to its proximity to the large negative sidelobes of the main continuum sources.

C7. This source appears to bridge the gap between C1/C2 and the Hot Core region, and little flux is lost with a $2''$ beam. However, 93% of the flux is lost with the subarcsecond A configuration beam, indicating that the small C7 source is surrounded by a large $\sim12'' \times 4''$ envelope.

C10. This source is detected with the $\sim2''$ C configuration beam with a source size of $\sim2'' \times 7''$; however, there is no flux lost when observing with a subarcsecond beam, indicating that the near point source may be embedded in a very diffuse envelope.

C11. This source is BN and is expected to be a point source, as can be seen by the fact that there is no flux lost from the lowest to highest resolution observations.

C13 and C14. These sources could not be individually resolved from surrounding sources in all but the A configuration, and so no additional properties can be inferred.

C15 and C16. Both of these sources appear to be embedded in an extended envelope, on the order of $\sim5''$. Over half of the flux is resolved out by a $2''$ beam, and a total of $\sim80\%$ is resolved out by the subarcsecond beam.
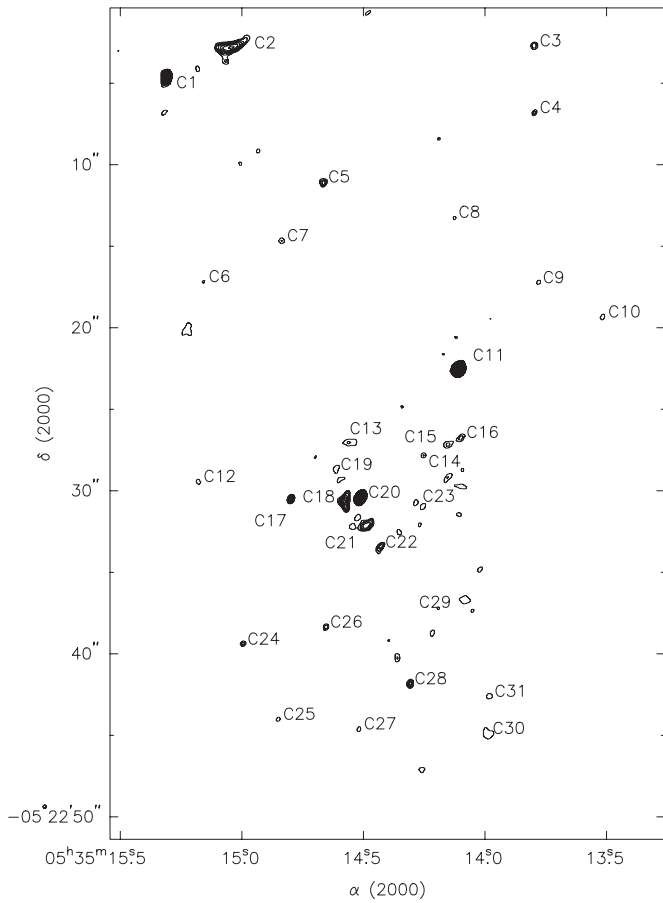
Figure 3. The A configuration continuum of the region with sources labeled according to the designations in Table 1. The contours are 9σ, 12σ, 15σ, ... ($\sigma = 280\,\mu$Jy beam^{-1}).

C17–C22. The individual sources could not be fully resolved by all but the highest resolution observations. Table 2 gives the fitted parameters for the B and C configurations; however, the errors are large due to source blending. The total flux of the complex (given in the last line of Table 2) shows that there is a notable large envelope surrounding all of the sources, over half of which is resolved out when observed with an $\sim 2''$ beam, and 82% of which is resolved out by the subarcsecond A configuration beam.

C23. This source, like many others, appears to be a near point source embedded in a surrounding envelope of a few arcseconds in size which produces nearly three quarters of the continuum flux.

C24. This source appears to be a point source with no surrounding envelope in all array configurations.

C28. The fit for this source from the A configuration data is poor, but based on the map flux it appears to be a point source with a minimal surrounding envelope.

C29. This source has notable extended flux, 75% of which is resolved out by a $\sim 2''$ beam. In the B configuration data this source appears as two distinct sources on either side of IRc5, only one of which is detected by the subarcsecond beam.

C30. This source was detected with all four array configurations but could not be resolved for fitting in the D configuration data. It appears to be a small source embedded in a weakly emitting surrounding envelope.

C32. This source was only detected in the C configuration and in the convolved A configuration data, indicating that it is a small source with a surrounding envelope that is below the detection threshold of the D and B configuration observations.
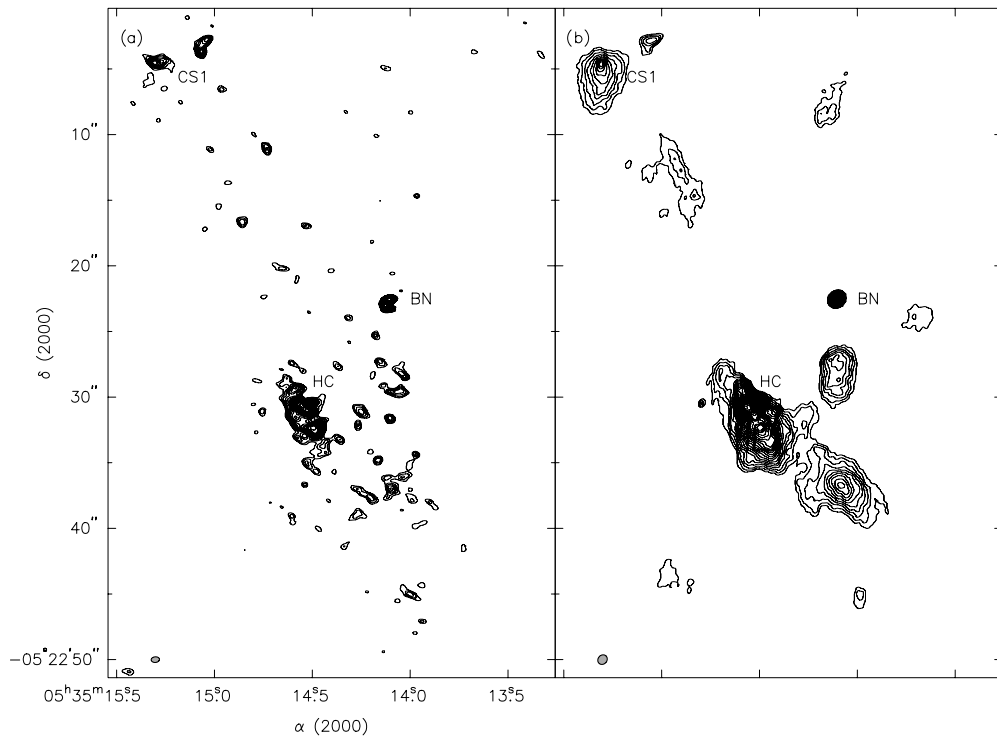
Figure 4. (a) Uniformly weighted map of all data. (b) Naturally weighted map of all data. Sources of interest are labeled (HC is Hot Core).

Table 2
Comparison of Fluxes of Continuum Sources

ID	D Configuration[a]	C Configuration[b]		B Configuration[c]		A Configuration[d]
	∫Flux (mJy beam^{-1})	∫Flux (mJy beam^{-1})	Size[e] ($'' \times ''$)	Resolved Out (%)[f]	Size[e] ($'' \times ''$)	Resolved Out (%)[f]
C1	⎫ 428.9 (14.7)[g]	152.9(6.7)	2.5 × 1.8	0	3.2 × 2.7	49
C2	⎭	98.8(4.5)	2.9 × 0.3	0	1.5 × 0.87	17
C3	. . .	. . .	. . .	. . .	. . .	. . .
C4	. . .	145.7(10.7)	7.2 × 2.8	. . .	. . .	75
C5	. . .	. . .	. . .	. . .	. . .	. . .
C6	. . .	. . .	. . .	. . .	. . .	. . .
C7	548.0 (22.4)	540.0(26.0)	12.6 × 4.4	. . .	. . .	93
C8	. . .	. . .	. . .	. . .	. . .	. . .
C9	. . .	. . .	. . .	. . .	. . .	. . .
C10	. . .	14.1 (0.9)	2.2 × 7.6	. . .	. . .	0
C11	100.0[h]	107.4 (2.1)	PS[i]	0	0.51 × 0.34	0
C12	. . .	. . .	. . .	. . .	. . .	. . .
C13	. . .	. . .	. . .	. . .	. . .	. . .
C14	⎫	. . .	. . .	. . .	. . .	. . .
C15	⎬ 611.8 (100.9)[j]	129.3(92.2)	5.2 × 1.1	. . .	. . .	40
C16	⎭	157.2(29.9)	2.5 × 2.2	. . .	. . .	. . .
C17	⎫	137.0(12.9)	3.5 × 2.9	. . .	. . .	. . .
C18	⎪	278.9[k]	5.0 × 4.2	47	1.4 × 1.2	. . .
C19	⎪	146.7[k]	4.0 × 2.9	88	. . .	. . .
C20	⎬ 913.1[l]	122.9[k]	PS[i]	43	0.69 × 0.39	. . .
C21	⎪	258.2[k]	5.1 × 3.7	51	0.80 × 0.66	. . .
C22	⎭	135.0[k]	3.3 × 3.0	19	1.3 × 0.57	. . .
C23	. . .	223.9 (5.8)	4.4 × 3.4	. . .	. . .	71
C24	. . .	14.4 (1.0)	PS[i]	0	PS[i]	. . .
C25	. . .	. . .	. . .	. . .	. . .	. . .
C26	. . .	. . .	. . .	. . .	. . .	. . .
C27	. . .	. . .	. . .	. . .	. . .	. . .
C28	. . .	17.2 (1.7)	PS[i]	. . .	. . .	. . .
C29	551.9 (181.9)[m]	112.5 (5.2)	3.2 × 2.0	0[n] ⎰	2.5 × 0.53	7
				⎱	2.0 × 0.8	
C30	. . .	80.4 (4.1)	2.5 × 0.8	0	. . .	30
C31	. . .	. . .	. . .	. . .	. . .	. . .
C32[o]	. . .	238.2 (8.1)	4.3 × 2.2	. . .	. . .	65
C33[p]	. . .	. . .	. . .	. . .	1.2 × 0.83	. . .
C34[q]	. . .	. . .	. . .	. . .	0.80 × 0.30	. . .
C18–C22[r]	913.2 (5.4)	829.3 (40.5)	. . .	46	. . .	82

Notes.
[a] Synthesized beam is $5''.9 \times 4''.9$.
[b] Synthesized beam is $2''.4 \times 2''.0$.
[c] Synthesized beam is $0''.96 \times 0''.85$.
[d] Synthesized beam is $0''.47 \times 0''.37$.
[e] Size was determined from the MIRIAD task IMFIT. Reported values are the deconvolved sizes.
[f] Percentage of the source flux that was resolved out in comparison to C configuration observations, 0% means no flux resolved out, 100% means all flux resolved out.
[g] At this resolution, C1 and C2 are completely unresolved, the reported integrated flux is from a single component fit.
[h] A reliable fit could not be obtained due to the large synthesized beam. The integrated flux was estimated from the peak intensity and expected point source size.
[i] The deconvolution resulted in a point source.
[j] The integrated flux is a summation of C14–C16, as the individual sources could not be resolved.
[k] Fit results were poor and no uncertainty was given.
[l] The integrated flux is a summation of C17–C22, as the individual sources could not be resolved.
[m] The integrated flux may include contributions from C23, as the individual sources could not be resolved.
[n] In the B configuration two sources are associated with C29 (see Figure 1), the resolved flux percentage is a combination of both sources.
[o] This continuum source was only detected in the C configuration; peak position is $05^h35^m14^s.070$, $-05°22'36''.581$.
[p] This continuum source was only detected in the B configuration; peak position is $05^h35^m14^s.613$, $-05°22'29''.688$.
[q] This continuum source was only detected in the B configuration; peak position is $05^h35^m14^s.464$, $-05°22'35''.350$.
[r] The values reported here are for a sum total from all continuum sources C18–C22.

C33 and C34. These sources were only detected in the B configuration and appear to be small, but larger than point-like sources.

A standard rule-of-thumb with molecular line observations in Orion-KL, based on the images presented by Liu et al. (2002), has been to assume an $\sim 5'' \times 5''$ spherical source structure
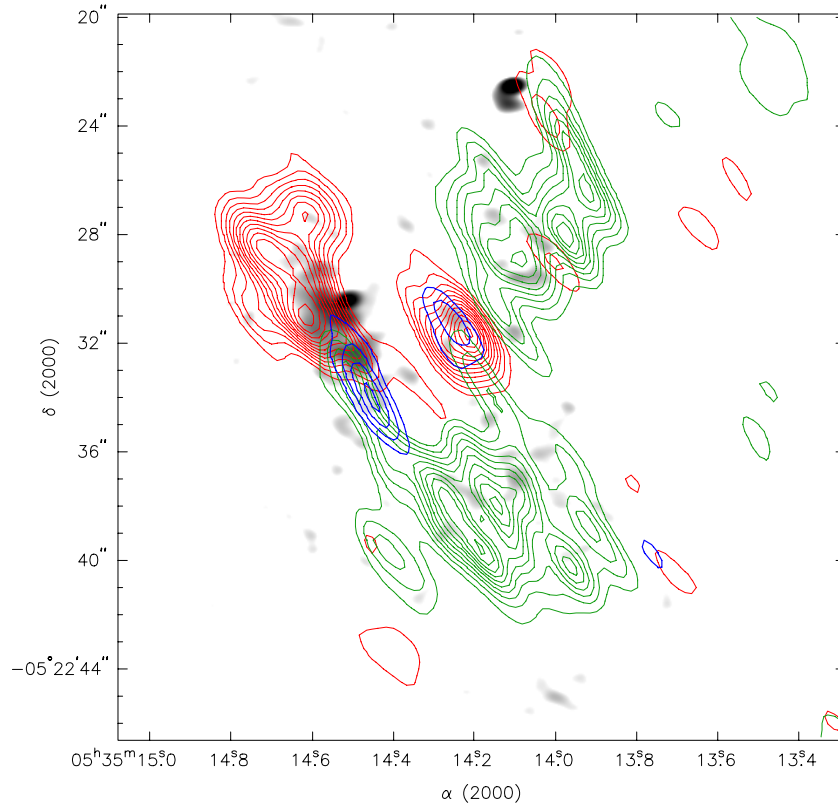
Figure 5. Molecular emission contours from (Friedel & Snyder 2008) overlaid on the grayscale continuum (uniformly weighted map). The continuum has been logarithmically scaled to show the weaker features in this high dynamic range image. The gray (red in online edition) contours are ethyl cyanide [C_2H_5CN], dashed (green in online edition) contours are dimethyl ether [$(CH_3)_2O$], and the black (blue in online edition) contours are acetone [$(CH_3)_2CO$].

(A color version of this figure is available in the online journal.)

for the Orion Hot Core, and an elongated $\sim5'' \times 10''$ oval source structure for the Compact Ridge. The results from the present work call into question this standard spatial model used to interpret Orion-KL molecular observations. These observations reveal that the Orion Hot Core and Compact Ridge are comprised of many bright but compact continuum sources that have not been spatially resolved in previous interferometric studies. These point sources are interspersed with regions of extended emission that are directly correlated with sources of heating and/or shocks. Given the complexity of the continuum morphology in this region, it is likely that the spatial distribution of molecular line emission will be similarly complex. Further evidence of this complex source morphology is shown in Figure 5, which compares the continuum images derived from this work to the molecular line images of Friedel & Snyder (2008). The grayscale traces the uniformly weighted continuum (logarithmically scaled to show the weaker features in this high dynamic range image), the gray (red in the online journal) contours trace ethyl cyanide [C_2H_5CN], the dashed (green in the online journal) contours trace dimethyl ether [$(CH_3)_2O$], and the black (blue in the online journal) contours trace acetone [$(CH_3)_2CO$]. This comparison reveals that significant source structure remains unresolved even with the $1''$ beam used in the Friedel & Snyder (2008) observations. This comparison also reveals that the continuum emission and molecular emission do not always necessarily trace the same source morphology. We conclude from this comparison that only direct, high spatial resolution observations for each individual molecule can be used to determine the true source morphology for that particular molecule. This information can then be used to accurately determine molecular abundances in the Orion-KL region.

4. SUMMARY

We have conducted extensive $\lambda = 3$ mm continuum observations of the Orion-KL star-forming region. These observations used the CARMA Array in four different array configurations to fully sample this region at varying spatial resolutions ($\sim0''.5$–$5''$ beams). It is apparent from these observations that the spatial distribution of the continuum in the Orion-KL region is much more complicated than has previously been considered. In the past, it has been routine to assume that there were two main sources of continuum in Orion-KL: the Hot Core/source I and source BN. In light of the results from the continuum observations reported here, this simplistic view of the Orion-KL structure must be revised. These observations show that these sources are comprised of nearly three dozen individual continuum sources, many of which appear to be point-like sources surrounded by extended envelopes. It would not be surprising for future higher spatial resolution observations to detect even more small continuum sources in the region. Comparison of these continuum maps to molecular maps from Friedel & Snyder (2008) reveal that high spatial resolution studies are required for each molecule detected in the Orion-KL region before a proper source structure model can be determined. Such studies will allow for more accurate determination of molecular abundances in the Orion-KL region.

REFERENCES

Becklin, E. E., & Neugebauer, G. 1967, ApJ, 147, 799
Beuther, H., Zhang, Q., Reid, M. J., et al. 2006, ApJ, 636, 323
Blake, G. A., Sutton, E. C., Masson, C. R., & Phillips, T. G. 1987, ApJ, 315, 621
Braz, M. A., & Epchtein, N. 1983, A&AS, 54, 167
Churchwell, E., Felli, M., Wood, D. O. S., & Massi, M. 1987, ApJ, 321, 516
Doi, T., O'Dell, C. R., & Hartigan, P. 2002, AJ, 124, 445
Eisner, J. A., & Carpenter, J. M. 2006, ApJ, 641, 1162
Eisner, J. A., Plambeck, R. L., Carpenter, J. M., et al. 2008, ApJ, 683, 304
Favre, C., Despois, D., Brouillet, N., et al. 2011, A&A, 532, 32
Feigelson, E. D., Broos, P., Gaffney, J. A., III, et al. 2002, ApJ, 574, 258
Friedel, D. N., & Snyder, L. E. 2008, ApJ, 672, 962
Garrod, R. T., Widicus Weaver, S. L., & Herbst, E. 2008, ApJ, 682, 283
Gaume, R. A., Wilson, T. L., Vrba, F. J., Johnston, K. J., & Schmid-Burgk, J. 1998, ApJ, 493, 940
Gezari, D. Y., Backman, D. E., & Werner, M. W. 1998, ApJ, 509, 283
Greenhill, L. J., Gezari, D. Y., Danchi, W. C., et al. 2004, ApJ, 605, L57
Johnston, K. J., Gaume, R., Stolovy, S., et al. 1992, ApJ, 385, 232
Laas, J. C., Garrod, R. T., Herbst, E., & Widicus Weaver, S. L. 2011, ApJ, 728, 71
Lada, C. J., Muench, A. A., Lada, E. A., & Alves, J. F. 2004, AJ, 128, 1254
Liu, S.-Y., Girart, J. M., Remijan, A. J., & Snyder, L. E. 2002, ApJ, 576, 255
Luhman, K. L., Rieke, G. H., Young, E. T., et al. 2000, ApJ, 540, 1016
Menten, K. M., & Reid, M. J. 1995, ApJ, 445, L157
Menten, K. M., Reid, M. J., Forbrich, J., & Brunthaler, A. 2007, A&A, 474, 515
Migenes, V., Johnston, K. J., Pauls, T. A., & Wilson, T. L. 1989, ApJ, 347, 294
Muench, A. A., Lada, E. A., Lada, C. J., & Alves, J. 2002, ApJ, 573, 366
O'dell, C. R., & Wong, K. 1996, AJ, 111, 846
Quan, D., & Herbst, E. 2007, A&A, 474, 521
Rieke, G. H., Low, F. J., & Kleinmann, D. E. 1973, ApJ, 186, L7
Sault, R. J., Teuben, P. J., & Wright, M. C. H. 1995, in ASP Conf. Ser. 77, Astronomical Data Analysis Software and Systems IV, ed. R. A. Shaw, H. E. Payne, & J. J. E. Hayes (San Francisco, CA: ASP), 433
Shuping, R. Y., Morris, M., & Bally, J. 2004, AJ, 128, 363
Simpson, J. P., Colgan, S. W. J., Erickson, E. F., Burton, M. G., & Schultz, A. S. B. 2006, ApJ, 642, 339
Wynn-Williams, C. G., Genzel, R., Becklin, E. E., & Downes, D. 1984, ApJ, 281, 172